

Flux-Activated Resonant Control of a Bosonic Quantum Memory

Fernando Valadares,^{1,*} Aleksandr Dorogov,^{1,*} Tanjung Krisnanda,¹ May Chee Loke,¹ Ni-Ni Huang,¹ Pengtao Song,^{1,†} and Yvonne Y. Gao^{1,2,‡}

¹Centre for Quantum Technologies, National University of Singapore, Singapore

²Department of Physics, National University of Singapore, Singapore

(Dated: February 23, 2026)

Universal control of bosonic degrees of freedom provides a hardware-efficient route for quantum information processing with high-dimensional systems. Bosonic circuit quantum electrodynamics (cQED), which leverages transmon ancillae to coherently control long-lived superconducting cavities, is well suited to this goal. However, the cavity transitions are nearly degenerate in the usual dispersive regime, which limits the direct addressability of individual excitation levels and increases the complexity of engineered gates. Here, we integrate an on-chip flux-control architecture with a long-lived bosonic memory housed in a 3D superconducting cavity to dynamically access resonant Jaynes–Cummings (JC) interactions, enabling universal control of the cavity field with an analytically simple protocol. We deterministically prepare Fock states and their superpositions by sequentially climbing the JC ladder, and realize efficient arbitrary rotations between any pair of Fock levels in the memory. This on-demand access to JC interactions offers a versatile toolbox for implementing robust Fock-basis qudits and harnessing the rich dynamics of high-dimensional bosonic elements for quantum information processing.

Effective control over a large Hilbert space is essential for both practical quantum information processing [1–3] and explorations of the rich underlying concepts of quantum physics [4–6]. The pursuit of progressively larger systems often takes the form of assembling collections of many interconnected and individually controlled two-level elements. This scaling incurs complex hardware overhead and imposes a significant challenge to current quantum technologies. One strategy to reduce hardware requirements is to use quantum systems that are intrinsically more complex, such as d -level systems (qudits) [7, 8]. This pathway has been explored in several platforms such as in molecular spins [9, 10], optical photons [11, 12], trapped ions [13, 14], silicon nuclear spins [15] and superconducting artificial atoms [16–18].

An alternative approach is to leverage the large Hilbert space of quantum harmonic oscillators. Notably, bosonic circuit QED systems use 3D superconducting cavities coupled to transmon ancillae to realize highly controllable and coherent oscillators. Such devices have demonstrated Fock state preparation up to 100 photons [19] and cat states with an average photon population of 1024 [20].

Universal control of the oscillator is typically achieved via dispersive coupling to a transmon qubit [21]. In this regime, cavity transitions are close in frequency (Fig. 1a) and not individually addressable. Therefore, arbitrary operations on the oscillator state often require driving the transmon and the cavity simultaneously with complex numerically optimized waveforms [22–24]. However, these numerical pulses are susceptible to parasitic dynamics, and their ‘black-box’ nature often complicates ef-

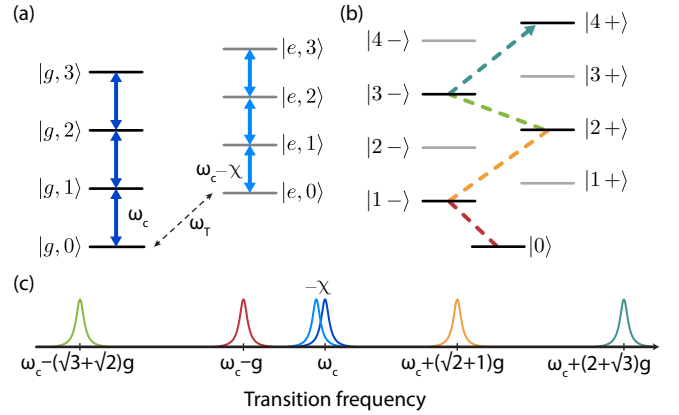


FIG. 1. **Comparison of the dispersive and resonant regimes.** (a) The bosonic transitions in the dispersive regime are degenerate within the each qubit manifold and are separated by $\chi \sim$ MHz between the $|g\rangle$ and $|e\rangle$ manifold. (b) This degeneracy is lifted in the resonant JC regime, with level splittings $\propto g \sim$ tens of MHz, enabling fast selective excitation of individual bosonic levels. (c) The frequency spectra of both coupling regimes shown on the same axis.

fective troubleshooting. Although control can also be implemented using higher-order parametric processes without numerical optimization [25, 26], they are limited by the achievable coupling strength or drive-induced errors [27, 28]. Developing analytical, versatile control methods that directly address individual cavity transitions would therefore fill an important gap for bosonic quantum information processing.

In this work, we use flux-activated resonant Jaynes–Cummings (JC) interactions to access number-selective cavity transitions and implement arbitrary yet analytically simple control of a bosonic memory mode. These dynamics are enabled by a dynamically adjusted

* Contributed equally to this work

† Current address: School of Automation Science and Engineering, Xi’an Jiaotong University, Xi’an 710049, China

‡ Corresponding author: yvonne.gao@nus.edu.sg

transmon-cavity detuning, which can shift the coupled system between a highly nonlinear resonant regime with well-resolved JC transitions and the dispersive regime with suppressed cavity photon loss. We protect the coherence of the bosonic memory against flux line leakage by incorporating on-chip low-pass filtering over the frequency band occupied by the cavity and the transmon. As a result, the lifetime of the bosonic mode reaches $T_1 = 590 \pm 40 \mu\text{s}$ ($Q = (2.6 \pm 0.2) \times 10^7$) when the transmon is tuned to be dispersively coupled – more than a two-fold improvement over previous implementations using the flux hose [29, 30]. We leverage these new capabilities to demonstrate the direct creation of Fock states and their superpositions by sequentially climbing the JC ladder (Fig. 1b). Furthermore, we achieve state transfer between any two chosen levels of the cavity by using multi-tone pulses and realize arbitrary rotations between them via simple analytical sequences. These results form the foundation for universal Fock-basis qudit control and robust quantum information processing using high-dimensional systems.

Our method to achieve universal control of the bosonic mode is based on adiabatically connecting the eigenstates of the resonant JC Hamiltonian to the product eigenbasis of the decoupled circuits [31]. The resonant JC Hamiltonian in the interaction picture is given by

$$\hat{H}_{JC} = g \left(\hat{a}^\dagger \hat{\sigma}^- + \hat{a} \hat{\sigma}^+ \right), \quad (1)$$

where $g = 12.2 \pm 0.1$ MHz is the coupling factor, \hat{a} (\hat{a}^\dagger) is the annihilation (creation) operator of the cavity and $\hat{\sigma}^-$ ($\hat{\sigma}^+$) is the lowering (raising) Pauli operators of the transmon taken as a two-level system. The \hat{H}_{JC} eigenstates are the ground state $|0\rangle$ and the N th-excited levels

$$|N\pm\rangle = \frac{1}{\sqrt{2}} \left(|N, g\rangle \pm |N-1, e\rangle \right), \quad (2)$$

where $|N, s\rangle$ is the product of the cavity Fock state $|N\rangle$ and the transmon state $|s = g, e\rangle$, with eigenfrequencies $\omega_{|N\pm\rangle} = \pm\sqrt{N}g$. This photon-number dependence of $\omega_{|N\pm\rangle}$ leads to the direct addressability of the transitions as illustrated in Fig. 1b.

We are particularly interested in the red and blue JC sidebands

$$\begin{aligned} |N+\rangle &\xleftrightarrow{\omega_{N,r}} |(N+1)-\rangle, \\ |N-\rangle &\xleftrightarrow{\omega_{N,b}} |(N+1)+\rangle, \end{aligned} \quad (3)$$

with transition frequencies $\omega_{N,r} = -\left(\sqrt{N+1} + \sqrt{N}\right)g$ and $\omega_{N,b} = \left(\sqrt{N+1} + \sqrt{N}\right)g$ relative to the rotating frame, respectively. This set of transitions, together with the ground state excitations $|0\rangle \leftrightarrow |1\pm\rangle$, can connect any two eigenstates of the resonant JC Hamiltonian with a high frequency selectivity scaling with g (Fig. 1c). When the transmon is adiabatically tuned out of resonance with the cavity to lower frequencies, the eigenstates in

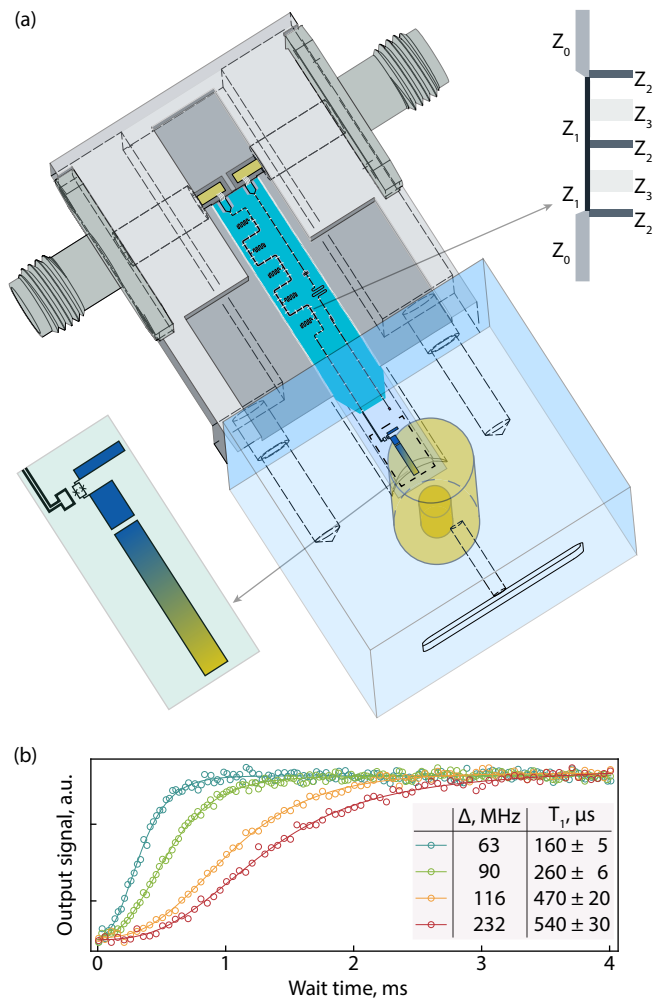


FIG. 2. Architecture for robust flux-delivery in a high-Q bosonic circuit QED device. (a) High-Q $\lambda/4$ coaxial cavity coupled to an asymmetric SQUID-transmon (shown in bottom-left inset). The flux bias is delivered by a transmission line wirebonded to an SMA port at the opposite end of the chip. The flux line and a readout resonator partially adopt a coplanar waveguide (CPW) architecture. They are equipped with two 3rd-order Chebyshev low-pass filters in series (schematics shown in top-right inset) and a Purcell filter, respectively, to protect the cavity and the transmon against decay. (b) The cavity T_1 is measured while the transmon is parked at a few selected flux points with different values of $\Delta = \omega_{cav} - \omega_T$, showing an increase of memory lifetime T_1 as the transmon-induced decay is mitigated at larger detunings.

Eq. (2) transform into products of cavity and transmon eigenstates: $|N+\rangle \rightarrow |N, g\rangle$ and $|N-\rangle \rightarrow |N-1, e\rangle$. The first sideband in Eq. (3) is transformed into the transition $|N, g\rangle \leftrightarrow |N, e\rangle$, which is available in standard dispersive regime [32]. In contrast, the blue sideband, $|N-1, e\rangle \leftrightarrow |N+1, g\rangle$, is only directly (using a single drive) accessible with the resonant JC dynamics [31]. Therefore, combining direct access to the resonant JC dynamics and the ability to adiabatically detune the qubit from the oscillator, we can orchestrate any desired bosonic mode.

To leverage this resonant control scheme, we construct a new bosonic circuit QED hardware that can simultaneously provide strong and broadband flux control while protecting the cavity from decay (Fig. 2a). Our device features a 3D superconducting cavity as the long-lived quantum memory, together with a lithographically defined on-chip flux line placed in close proximity to the SQUID loop with mutual inductance of $0.387 \Phi_0/\text{mA}$ with the SQUID loop ($470 \mu\text{m}^2$) and an average magnetic field of $1.70 \mu\text{T}/\text{mA}$. This highly effective flux delivery structure allows to minimize the loop area and hence reduce the impact of flux-noise on the transmon coherence times [33]. In this particular device, we measure transmon $T_1 \approx 23 \mu\text{s}$ and $T_2^{\text{echo}} \approx 3.5 \mu\text{s}$ in the lower sweet spot. The flux line bandwidth is measured to be at least 1.3 GHz, potentially limited by a low-pass filter on the line [33], allowing fast transmon frequency adjustment in the nanosecond timescale. This device provides a more compact alternative to the microstrip flux line design shown in recent work [34], allowing more convenient integration of additional circuits such as the readout resonator and cascaded filtering on the same chip.

The configuration of our CPW-based filtering structure is carefully optimised to reduce the energy loss of cavity and transmon through the flux line. We use two 3rd-order low-pass Chebyshev filters [35] in series and based on finite element simulations, they achieve 98 dB attenuation at the cavity frequency of $\omega_{\text{cav}}/2\pi = 6.868 \text{ GHz}$ and at least 50 dB attenuation in the transmon frequency range of $\omega_T/2\pi = 5.894 - 7.634 \text{ GHz}$. As a result, energy loss through the flux line is heavily suppressed for both quantum memory and transmon. We verify this by preparing the cavity in a coherent state and tracking the vacuum state $|0\rangle$ population over time at a few different cavity-transmon detunings as shown Fig. 2b. The lifetime reaches a maximum of $T_1 = 590 \pm 40 \mu\text{s}$ at a detuning of $\Delta = \omega_{\text{cav}} - \omega_T = 2\pi \times 260 \text{ MHz}$, at which point the inverse-Purcell decay is suppressed. These photon loss values are comparable to those of typical 3D bosonic superconducting devices without flux integration.

Our device combines a highly coherent bosonic mode with fast tunability of a nonlinear ancillary element, making it an ideal testbed for resonant control protocols. We first showcase the efficacy of this control framework by preparing arbitrary superpositions of Fock states with a set of analytical pulses. For example, we prepare $\frac{1}{\sqrt{2}}(|0\rangle + |3\rangle)$ (Fig. 3a) using a pulse sequence consisting of a $\pi/2$ -pulse from $|0\rangle$ to $|1+\rangle$ followed by two π -pulses to $|2-\rangle$ and $|3+\rangle$. The frequencies of each transition are determined using standard spectroscopy experiments, and the pulses durations are chosen to maximize the photon-number parity contrast after climbing each step of the JC ladder [33]. The optimal speed of the adiabatic detuning is calibrated by preparing $|1+\rangle$ on resonance, applying a flux pulse with a smooth, variable-duration ramp until $\Delta = 100 \text{ MHz}$, and then measuring the cavity $|1\rangle$ population with a photon-number-resolved spectroscopy. We pick a minimal ramp duration of 200 ns

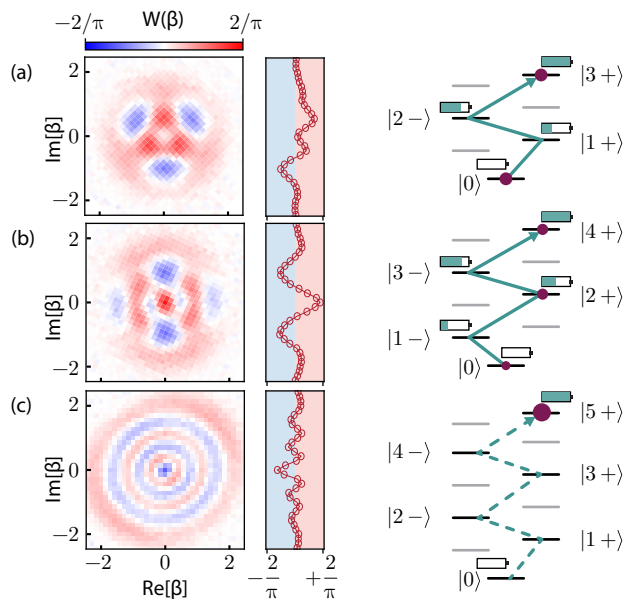


FIG. 3. **State preparation in the resonant regime.** Wigner tomography and a 1D cut along $\text{Re}[\beta]$ of states created using the flux-activated resonant interactions, together with corresponding steps activated to excite the JC ladder. (a) state $\frac{1}{\sqrt{2}}(|0\rangle + |3\rangle)$, and (b) state $\frac{1}{2}|0\rangle + \frac{\sqrt{3}}{8}(i|2\rangle + |4\rangle)$ are created using sequential drives. (c) Fock $|5\rangle$ created from vacuum by simultaneously driving multiple JC transitions.

for which $|1\rangle$ population is maximum. We apply the same method to create $\frac{1}{2}|0\rangle + \frac{\sqrt{3}}{8}(i|2\rangle + |4\rangle)$ (Fig. 3b), where the phase of the superposition is implemented by simply changing the phase of the pulse addressing this transition. The total pulse sequence to prepare the state in Fig. 3a (b) takes 640 ns (688 ns), and the corresponding fidelity of the final state is estimated as $93 \pm 3\%$ ($89 \pm 2\%$) from density matrix reconstruction [36, 37], limited by transmon decoherence [33].

As an alternative to sequentially climbing the JC ladder, several transitions can also be activated simultaneously to realize more complex dynamics. For instance, the analog of the spin angular momentum J_x over a subspace of dimension d of the JC Hamiltonian can be constructed by driving each transition with amplitude

$$A_n = 2\eta_n A \sqrt{n(d-n)}, \quad 1 \leq n < d, \quad (4)$$

where A is the overall pulse amplitude and η_n is an experimentally calibrated scaling factor of the drive strength associated to each transition [33]. Driving J_x for a total time of π/A enacts pairwise state transfers between target levels. Here we use this multi-tone drive to create Fock $|5\rangle$ from the ground state. We allow A_n to assume complex values and obtain the amplitudes using a gradient descent algorithm which maximizes the state preparation fidelity for a fixed time [31, 33]. We present, in Fig. 3c, the measured Wigner function of a Fock $|5\rangle$ prepared with this method using a 800 ns pulse. We obtain

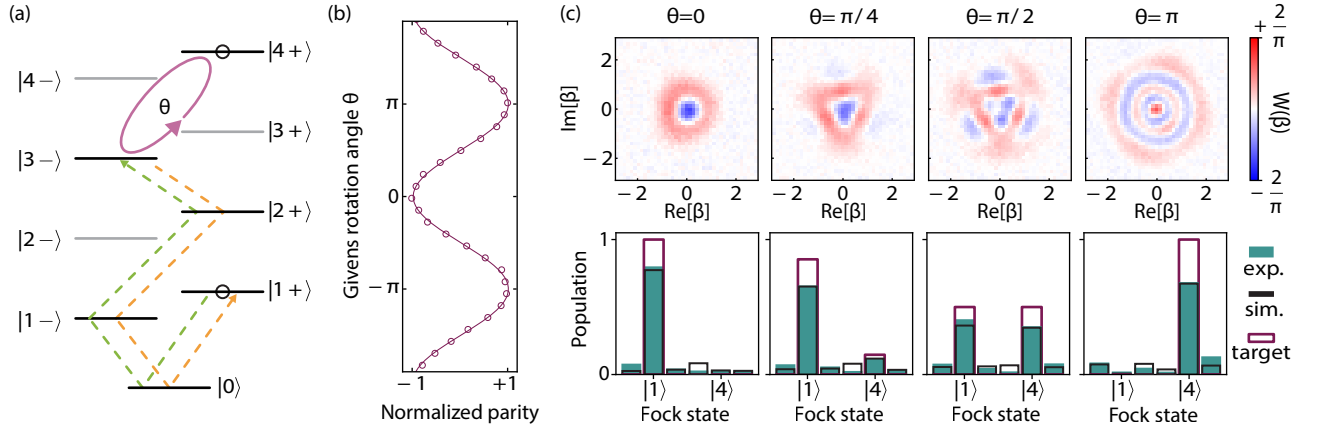


FIG. 4. **Givens rotations between two Fock levels.** (a) The $|1+\rangle$ state population is swapped with $|3-\rangle$ state using a J_x pulse, which is then followed by a sideband pulse to $|4+\rangle$ and a second J_x pulse that reverts the first swap. This sequence effectively implements an operation between states $|1+\rangle$ and $|4+\rangle$ that translates into a Givens rotation between Fock states $|1\rangle$ and $|4\rangle$ after adiabatic detuning. (b) Measurement of the normalized final state parity for arbitrary rotation angle θ from an initial state $|1\rangle$, showing the protocol can create arbitrary superpositions of the two Fock states. (c) Wigner plots and Fock states populations obtained from the reconstructed density matrices of the cavity state for $\theta = 0, \pi/4, \pi/2$ and π . The measured population distribution agrees well with the simulated results with real experimental parameters.

a state fidelity of $75 \pm 2\%$, limited by both the transmon decoherence and imperfection calibrations of η_n [33].

Additionally, we use the multi-tone control to apply arbitrary rotations between two Fock levels. The protocol consists of resonantly transferring the population of a level $|n_{A+}\rangle$ to $|(n_B - 1)-\rangle$, and then driving a transition from the latter state to $|n_{B+}\rangle$ with an effective rotation angle θ (Fig. 4a). The sequence is concluded with a second J_x applied in reverse, which swaps $|(n_B - 1)-\rangle$ and $|n_{A+}\rangle$ populations while reverting spectating levels to their original configuration. After the transmon is adiabatically detuned, this operation is equivalent to a Givens rotation between the cavity levels $|n_A\rangle$ and $|n_B\rangle$ [38]. We show the efficacy of this protocol by applying Givens rotations between Fock state $|1\rangle$ and $|4\rangle$. The parity of the final state is measured as a function of θ , showing a continuous evolution between a minimum value corresponding to $|1\rangle$ and a maximum corresponding to $|4\rangle$ (Fig. 4b). For $\theta = 0, \frac{\pi}{4}, \frac{\pi}{2}$ and π , we measure the full Wigner function of the cavity as shown in the plots in Fig. 4c. The density matrix reconstruction of the Wigner measurements indicates state fidelities of $80 \pm 2\%$, $76 \pm 2\%$, $71 \pm 2\%$, $68 \pm 2\%$, respectively. This is consistent with the numerical simulation using real experimental parameter [33].

The performance of the Givens rotation and state preparation are estimated to be limited by transmon dephasing, followed by comparable contributions of T_1 and coherent errors [33]. The effect of each decoherence channel can be understood in terms of the overlap of JC levels with the corresponding jump operators. The transmon pure dephasing, described by σ_z , translates into a depolarization within each excitation manifold as $\langle N \pm | \sigma_z | N \mp \rangle = 1$, without introducing pure dephasing as $\langle N \pm | \sigma_z | N \pm \rangle = 0$. In the limit

of the long coherence times of the memory mode, the transmon loss dominates the JC level relaxation. Under this condition, photon loss events are described by $\langle (N - 1) \pm | \sigma^- | N \pm \rangle = \langle (N - 1) \mp | \sigma^- | N \pm \rangle = 0.5$, leading to an effective JC lifetime twice that of the transmon T_1 , and which does not suffer from bosonic enhancement at higher excitation levels. The modest coherences of this particular transmon also limits the duration of the individual JC drives, which in turn results in coherent leakages due to limited selectivity. A full master equation simulation using these error models is consistent with the experimental observations [33].

There are several known strategies to mitigate the decoherence of flux-tunable transmons that can be adopted to enhance the fidelity of the resonant protocol. For example, the transmon T_2 can be increased by reducing the flux sensitivity of the SQUID, either by decreasing its area, increasing the asymmetry between the shunting Josephson junctions [33, 39], or using geometries that are inherently more noise-resilient [40]. At the same time, flux modulation can be used to engineer AC sweet spots at the cavity frequency to reduce the direct decoherence limit during the operations. Both strategies are supported by the large bandwidth and strong flux delivery of the on-chip line developed in this work. Besides greater T_2 , increasing the transmon-cavity coupling strength g leads to more selective sideband transitions and faster adiabatic detuning, both of which can reduce the duration of the protocol and mitigate errors. Thus, the performance of the resonant operations shown in this work is not fundamentally limited by the control mechanisms or our device architecture, and can be directly improved by further optimization of device parameters.

In summary, our work demonstrates the control of a long-lived bosonic quantum memory through

number-selective transitions in the JC Hamiltonian. This new capability is enabled by a robust flux-tunable architecture that can effectively switch the system between the dispersive and the resonant regimes. We prepare arbitrary superpositions of Fock states via either sequential or multi-tone sideband driving. Moreover, we use efficient state swapping gates to implement arbitrary Givens rotations, providing a path for the universal control of Fock-basis qudits encoded in oscillators [38]. This approach potentially enables the realization of high-dimensional qudits without the increasingly significant charge dispersion that affects higher levels of transmon-based implementations [16]. Furthermore, the resonant control demonstrated here is favorable compared to numerically optimized protocols [23, 24, 41]: in our scheme, the control parameters depend on a finite set of frequencies and amplitudes that can be individually calibrated to high precision without requiring a classical computation step. Additionally, the operations are implemented in a closed subspace, avoiding excursions to higher photon numbers that may amplify loss and nonlinear distortions. Finally, due to the direct access to the JC levels, our protocol leverages a frequency selectivity that scales with the coupling factor g , allowing much faster operations compared to other demonstrations of analytical multi-level cavity control [25, 42]. Therefore, our work marks an important contribution to the control capabilities of long-lived microwave cavities in circuit QED and opens up new possibilities for quantum information processing with bosonic modes.

Acknowledgments We acknowledge the funding support from the Singapore Ministry of Education (T2EP50222-0017) and The University of Sydney - National University of Singapore 2026 Ignition Grants. F.V., A.D., N.H., acknowledge the support of the Singapore National Quantum Scholarship Scheme (NQSS). We thank Mr. Kyle Chu and Mr. Jean-Samuel Tettekpoe for their technical inputs during the project development.

SUPPLEMENTARY MATERIAL

I. DEVICE DESIGN

The standard bosonic cQED architecture consists of a high-Q bosonic mode hosted in a 3D superconducting cavity with convenient control and measurement tools provided by an on-chip ancillary transmon and a planar low-Q readout resonator. Our device extends this design by integrating fast-flux tunability without compromising long cavity lifetimes.

These flux control features are achieved by combining coplanar waveguide (CPW) and microstrip line architectures. We show the details of the circuit in Fig. 5. The tunable transmon is designed in a microstrip geometry, allowing it to have a large dipole moment that couples strongly with the cavity. The SQUID loop of the transmon is inductively coupled to an on-chip coil biased by a CPW flux line. The flux line is designed with an integrated microwave low-pass filter that mitigates cavity and transmon photon loss.

In this section, we explain the technical specifications and design considerations of the tunable transmon and the flux line control.

A. Tunable transmon with asymmetric SQUID

Standard transmon [43] qubits feature nonlinear inductance implemented as a Josephson junction, leading to anharmonic oscillator spectrum where one can isolate two-dimensional computational subspace with the transition frequency ω_T given by

$$\hbar\omega_T = \sqrt{8E_C E_J} - E_C, \quad (5)$$

where E_J and E_C stand for Josephson and capacitive energies, respectively.

In order to make such a qubit tunable, single Josephson junction should be replaced by a loop with two junctions in parallel, forming a SQUID. Magnetic flux Φ_e threaded through the SQUID loop effectively changes the value of the inductance and, therefore, the qubit frequency, according to

$$\hbar\omega_T = \sqrt{8E_C \cdot 2E_J |\cos \varphi_e|} - E_C, \quad (6)$$

where E_J is the Josephson energy of a single junction, $\varphi_e = \pi \frac{\Phi_e}{\Phi_0}$ the normalised flux, and Φ_0 the magnetic flux quantum. Typical spectrum of ω_T as a function of the applied magnetic flux is shown in Fig. 6(a).

In such tunable devices, noise in the DC bias or in the magnetic environment lead to the fluctuations of the magnetic flux. This, in turn, varies the transmon frequency and leads to significant limitations on the T_2 lifetime. Thus, it is beneficial to operate at the sweetspots, where the qubit is first-order insensitive to the flux noise.

At other bias points, the qubit suffers rapidly increasing dephasing.

This sensitivity to the flux noise can be quantified as $\frac{\partial \omega_T}{\partial \Phi_e}$, i.e. how much the qubit frequency reacts to fluctuations of the magnetic flux due to the noise. From Eq. (6),

$$\frac{\partial \omega_T}{\partial \Phi_e} = -\frac{\pi^2}{\Phi_0} \sqrt{2 \frac{E_C \cdot 2E_J}{h^2} \frac{\sin 2\varphi_e}{\cos^{\frac{3}{2}} \varphi_e}}. \quad (7)$$

The sensitivity to flux noise grows rapidly outside of the sweetspots due to the strong frequency dependence on the applied flux bias. Here, we intentionally suppress this dependency by making the two junctions asymmetric, i.e. having different Josephson energies [39]. The extent of asymmetry is expressed as

$$\gamma = \frac{E_{J2}}{E_{J1}}, \quad (8)$$

where E_{J1} and E_{J2} are Josephson energies of the junctions and $\gamma > 1$ without loss of generality.

Naturally, the spectrum of the asymmetric transmon will also depend on parameter γ :

$$\hbar\omega_T = \sqrt{8E_C \cdot E_{J1} \sqrt{\gamma^2 + 2\gamma \cos 2\varphi_e + 1}} - E_C. \quad (9)$$

We calculate the flux noise sensitivity analogously to Eq. (7) using sing (9) and obtain

$$\frac{\partial \omega_T}{\partial \Phi_e} = -\frac{\pi^2}{\Phi_0} \sqrt{\frac{2E_C E_{J1}}{h^2}} \frac{4\gamma \sin 2\varphi_e}{(\gamma^2 + 2\gamma \cos 2\varphi_e + 1)^{\frac{3}{4}}}. \quad (10)$$

To compare, we present the simulated flux sensitivities obtained using Eq. (7) and Eq. 10 in Fig. 6(b). One can observe that more asymmetric transmons are less sensitive to the flux noise at the expense of a smaller frequency range. Therefore, for this particular device, we designed the SQUID to be asymmetric with a parameter $\gamma = 4.02$. The resulting frequency range is 5.894 - 7.634 GHz, as shown in Fig. 7(a).

It is worth mentioning that Eq. (6) and further analysis, strictly speaking, is only valid for the applied biasing DC current. In case of a AC flux drive, a more rigorous analysis [28, 44] must be applied to ensure an effective differential drive on the SQUID. This optimization can be further complicated by the use of an asymmetric SQUID. although it is outside of the scope of this work, we are actively exploring alternative strategies that can balance the robustness to flux noise with the effective suppression of the common mode drive for future works that require clean AC modulation of the qubit frequency.

B. Flux line & on-chip microwave low-pass filter

The integration of on-demand adjustment of the transmon frequency without reducing the cavity coherence

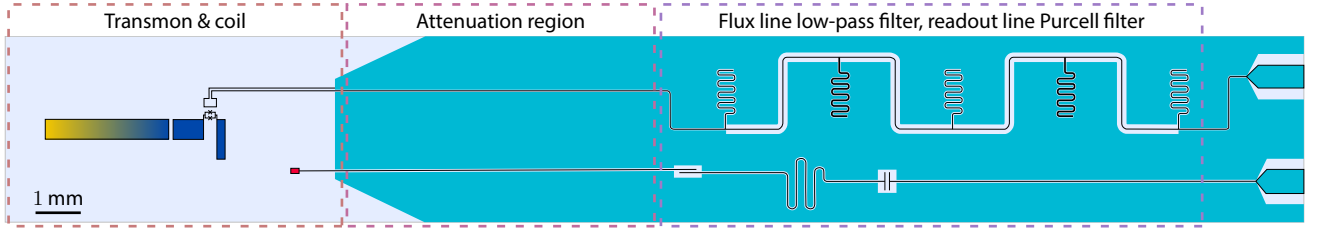


FIG. 5. **Chip schematic.** It features ancilla DC-SQUID transmon, low-Q readout resonator with Purcell filter, and on-chip flux line with microwave low-pass filter

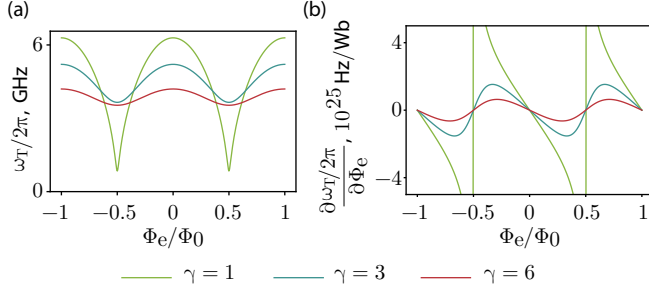


FIG. 6. **Reduced noise sensitivity of asymmetric SQUID transmons.** (a) Frequency response for variable junction asymmetry factors γ . (b) Calculated transmon frequency sensitivity to flux noise as a function of flux bias.

times had been an outstanding challenge for the bosonic cQED community. This feature is crucial as it enables powerful quantum information processing protocols [31, 45], as well as new opportunities for quantum simulation [46, 47] and quantum machine learning [48, 49]. However, initial attempts of the implementation of the broadband on-chip flux line encountered an issue of compromising cavity coherence [50]. In recent efforts, alternative ways of the flux delivery to the SQUID loop of the tunable ancilla have been explored [29, 30, 51]. However, these implementations tend to be difficult to manufacture reproducibly and offer limited bandwidth (~ 100 MHz).

In this work, we demonstrate the device that combines an on-chip flux line with both effective DC and AC flux delivery with a long-lived cavity. That is achieved by implementing heavy filtering of the flux line: we incorporate compact, third order Chebyshev low-pass filter [35] on the same chip. To ensure effective filtering performance and protection of the cavity mode, we concatenate two such filters, with the stub Z_2 shared between the two, as depicted schematically in Fig. 5. We leverage the CPW architecture, which allows to reach necessary impedances in much more compact design compared to the microstrip analogue [34], to fit both filtering stages on the 4.1 mm-wide chip. Moreover, our CPW architecture also suppresses cross-talk between the flux and readout modes hosted on the same chip.

The impedance values of the series inductances and

stub capacitances used in our filter are listed in Tab. I, along with the corresponding CPW line dimensions.

Section	Impedance, Ω	Conductor width, μm	Gap width, μm
Z_0	50	11	5
Z_1	130	5	100
Z_2	81	5	13
Z_3	46	15	5

TABLE I. **Impedances of the 3-rd order Chebyshev low-pass filter.** Filter diagram is shown in Fig. 2 (a) of the main text.

The simulated response of the on-chip low-pass filter is shown in Fig. 7 (b). The attenuation at the cavity frequency (6.868 GHz) is 98 dB. For the entire transmon frequency band, the attenuation is at least 50 dB.

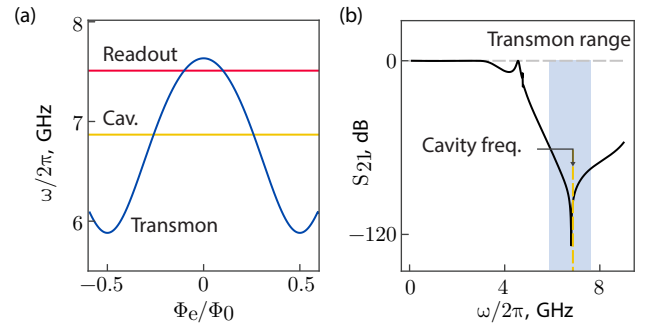


FIG. 7. **Filtering and spectrum.** (a) A spectrum of the transmon with asymmetric SQUID. Cavity and readout resonators frequency are shown. (b) S_{21} parameter of the cascaded low-pass 3-rd order Chebyshev filter.

In this device, the SQUID area is $470 \mu\text{m}^2$ (Fig. 8(a)), and the flux line coil loop is placed as close as $58 \mu\text{m}$ away from it to maximize the coupling (Fig. 8(b)). **The mutual inductance of $L_{DC} = 0.387 \Phi_0/\text{mA}$** is measured from the transmon frequency periodicity with a DC bias. This allow us to reach full tunability (requires $\Phi_e = \frac{1}{2}\Phi_0$) with only 1.292 mA DC bias, which does not cause any measurable heating of the transmon.

Furthermore, we incorporate a long constriction in the volume where the chip is housed, which we dub the "attenuation region". It considerably increases the cutoff

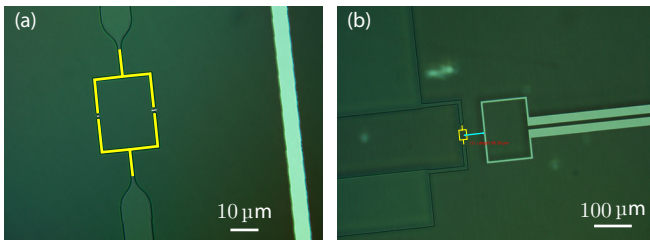


FIG. 8. **Optical images of the device after electron beam lithography.** (a) SQUID loop (yellow) with asymmetric junctions (white). (b) Flux line coil, biasing the transmon.

frequency of the waveguide structure, enhancing the suppression of the cavity field traveling outside the ground plane. Hence, the cavity field can only reach the drive ports through the CPW mode, which is heavily filtered.

C. Readout and Purcell filter

Another advantage of the compactness of CPW architecture, realised with the hybrid chip design, is simplicity in integration the readout resonator and the associated the bandpass Purcell filter on the same chip. Our Purcell filter, which is shown in Fig. 5, is strongly coupled capacitively to both the readout resonator and the feed line. With this design, our readout resonator, which we place at 7.51 GHz, has coupling $Q \approx 700$ without introducing any notable limitations on the the transmon Q factor.

II. DEVICE FABRICATION

As the device used in this study has considerably larger footprint to the ground plane and the flux line with low-pass microwave filter, compared to typical transmon chips used in bosonic cQED devices. For practical purposes, we only EBL for the transmon pattern and photolithography for all other the parts on the chip, as summarised in the table below.

An optical microscope image of the SQUID right after EBL exposure is shown in Fig. 8(a).

Step 1: alignment markers

The fabrication of the device begins with the cleaning of a 2-inch C-plane sapphire wafer by sonicating for 4 minutes each in N-Methyl-2-pyrrolidone (NMP) and methanol, followed by baking at 200°C for 5 minutes to remove any residual water molecules. Following this, the wafer is cooled down on a heat sink for 5 minutes. After that we spincoat two layers of the EBL resists: 550 nm of MMA (8.5) MAA EL13 and 250 nm of 950k PMMA A4. Each of the spincoating rounds is followed by baking for 5 minutes at 200°C. Next, we sputter ~ 10 nm

anti-charging gold layer. We then expose the alignment markers using Raith EBPG 5200+ EBL system with the dose $750 \mu\text{C}/\text{cm}^2$. Subsequently, we etch gold using KI gold etchant and develop the exposed pattern with 3:1 IPA:H₂O at 6°C for 2 minutes.

In the following step, we etch the surface for 60 seconds in Ar (85%) – O₂ (15%) environment and evaporate 115 nm of Nb using Angström Engineering double-angle evaporation system. We perform lift-off soaking the wafer in NMP at 90°C for 3 hours and then sonicating in NMP, acetone and methanol 3 minutes each.

Step 2: readout line, flux line, ground plane

We start by spincoating $\sim 1 \mu\text{m}$ of AZ1512 photoresist and baking for 1 minute at 100°C. Once that is complete, we expose the large features with 405 nm laser in Durham Magneto Optics MicroWriter ML3 Pro. Following this, we develop the exposed resist with MF-319 developer for 40 seconds and evaporate 100 nm of Al. Aluminium evaporation is followed by capping in 20 mbar O₂ environment for 20 minutes. To lift-off, we soak the wafer in NMP at 80°C for 4 hours and sonicate in NMP, acetone and methanol 3 minutes each.

Step 3: transmon with SQUID

Finally, we perform standard electron beam lithography to make the trasmon qubit. The junctions are fabricated using the bridge-free technique, presented in [52]. We then perform double-angle evaporation by first etching the resist at $\pm 20^\circ$ angles for 15 seconds each. Subsequently, we deposit two layers of Al with thickness of 20 nm and 40 nm Al, separated by oxidation for 20 minutes in 20 mbar O₂ environment. We finish the evaporation by capping in 20 mbar O₂ environment for 20 minutes.

III. DEVICE ASSEMBLY AND WIREBONDING

A. Package

Conventional bosonic cQED architecture usually using a monolith package, made of high-purity aluminium, to minimize seam loss [53, 54]. The chip hosting the ancillary elements is inserted into a waveguide to couple capacitively to the cavity mode and the other end of the chip is held by a clamp, which is, in turn, attached to the main package. However, this approach is not suitable for the device we use here. The on-chip ground plane and requirement for wirebonding necessitate a seam placed near the cavity wall.

Hence, our superconducting package was carefully re-designed to accommodate these requirements. Unlike conventional architecture, our package consists of three

# of lithography step	Exposure method	Material	Written feature
1	EBL	Nb	Alignment markers
2	Photolithography	Al	Readout line, flux line, ground plane
3	EBL	Al	Transmon with the SQUID loop

TABLE II. **Summary of main fabrication steps.** A breakdown of the processes used in fabricating respective on-chip features.

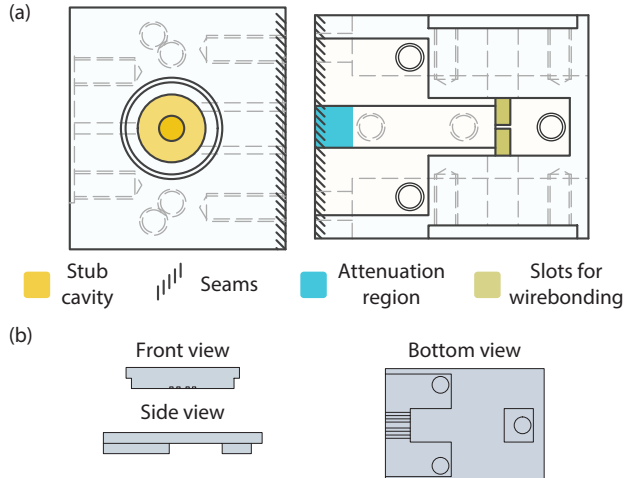


FIG. 9. **Design of the superconducting package.** (a) Top view of the main body and the bottom clamp. (b) Design of the top clamp with engineered constrictions that reduces the participation of the cavity field near the ground plane of the chip.

separate parts. The main body contains the cavity and the circular waveguide, where the transmon is inserted (Fig. 9(a)). This part is made of 4N6 aluminum to ensure the lifetime of the coaxial $\lambda/4$ -cavity.

The waveguide and clamping structures consist of two pieces, the bottom and top clamps. As we expect the high-Q cavity mode field to be weak in the clamps volume, these parts are made of 6061 aluminum alloy to allow more precise machining and mechanical robustness.

The top clamp functions as a lid that covers the chip and shields it from the environment. Importantly, it features a 4mm-long extrusion (Fig. 9(b)), which blocks the cavity field from propagating towards SMA ports outside the heavily filtered CPW line.

The bottom clamp features a 0.5 mm-deep pocket, where the chip is located (Fig. 2(a), main text). We use wirebonding to connect the on-chip ground to the surface of the clamp surrounding it (Fig. 10(a),(c)). The package is then mounted on the MXC flange of the dilution refrigerator, effectively connecting on-chip ground plane to the common fridge ground. Similarly, we use wirebonding to galvanically connect the flux and readout line terminals to flat beryllium-copper pins, that are connected to SMA ports (Fig. 10(b)). The drive signals are supplied to the SMA ports through the coaxial lines of the dilution refrigerator.

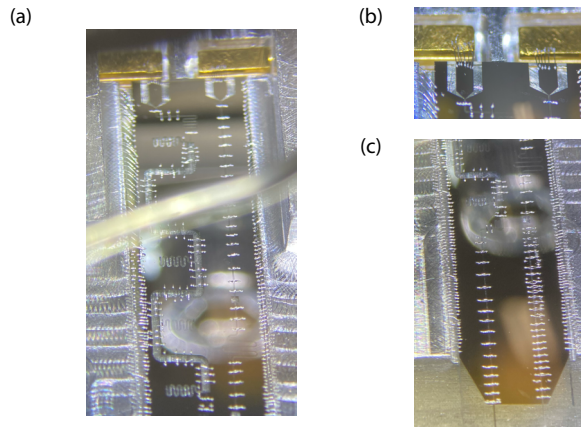


FIG. 10. **Wirebonding.** (a) Image of the chip on the bottom clamp after wirebonding. (b) Connection of the on-chip lines to SMA ports. (c) Bond wires and galvanic connection between the on-chip ground plane and the aluminum bottom clamp are also realised with wirebonding.

Seam losses estimation

To avoid deterioration of the cavity lifetime, our design places the seam as far as possible from the cavity. In order to estimate cavity Q-factor due to the seam loss, we integrated the cavity field over a 0.4 mm-wide ribbon along the seam. Even though we don't have exact data on the loss tangent of the seam, we could use that method to optimize the design based on the relative changes of the cavity Q.

Distancing the seam comes at the cost of increasing the separation between the cavity and the transmon, which could lead to decreasing their coupling strength g . In order to mitigate this effect, we implemented a microstrip structure to extend the transmon field and recover some of the capacitive coupling, similar to the design used in Ref. [29].

B. Assembly

We begin the assembly by putting a small amount of the Apiezon N cryogenic vacuum grease on the surface of the bottom clamp. We then place the chip on top and press slightly with a wooden part of the cotton swab. The grease is only present at the back part of the chip, far from the cavity.

Next, the top clamp is placed on top of the chip and

fastened with 3 screws. At this point, the chip is extruding out of the clamp slightly. Finally, the cavity body and the clamping pieces are attached together with the two screws located at the bottom of the clamp.

To improve the contact at the seam in our package, we put indium wire in between the cavity and clamping parts. The quality of this joint can be further improved with welding [20] or more advanced surface treatment [55].

Before mounting the device on the MXC flange of the dilution refrigerator, we cover all the seams between the parts with aluminum tape to ensure that the package is light-tight.

IV. CALIBRATION OF TRANSITIONS

The Jaynes-Cummings ladder has a rich spectrum of transitions. We calibrate the frequency and amplitude of each transition by preparing the system in one of the adjacent states and then performing spectroscopy and Rabi oscillation experiments, respectively.

To calibrate the $|3-\rangle \leftrightarrow |4+\rangle$ transition, for example, the system is initialized in $|3-\rangle$ with the cavity and transmon in resonance. The transmon is then driven by a pulse with variable frequency and subsequently adiabatically detuned from the cavity. Finally, the transmon, now dispersively coupled to the cavity, is used to measure the parity using a standard Ramsey sequence. A change in parity indicates that drive has excited one of the four allowed transitions to states $|2\pm\rangle$ or $|4\pm\rangle$, which appear as four well-resolved features in the spectroscopy diagram. The desired $|3-\rangle \leftrightarrow |4+\rangle$ transition is identified as the one with highest frequency, in accordance to the theory.

After the transition frequency is identified, the amplitudes of excitation pulses are calibrated with power Rabi experiments. A gaussian pulse with standard deviation σ and a total duration of 4σ is applied to the transmon line with variable amplitude. The amplitude corresponding to a π pulse is the point in which the parity of the system is changed from odd to even. This experiment allows us to calculate the Rabi frequency Ω_s of the effective drive $\frac{\Omega_s}{2}|4+\rangle\langle 3-|$. The corresponding frequencies and amplitudes of each JC transition are calibrated using this method and summarized in Tab. III.

We use this method to calibrate the gaussian excitation pulses used for cavity state preparation in the main text (Tab. III). The σ of each pulse was swept while tracking the parity of the state after a 2π rotation. The ideal σ is that in which the parity of the final state is as close as possible to the parity of the initial state. This corresponds to a compromise between the leakage and decoherence errors that affect short and long pulses, respectively.

Transition	$\omega_s/2\pi$ (GHz)	$\Omega_s/2\pi$ (MHz)	σ (ns)
$ 0\rangle \leftrightarrow 1+\rangle$	6.8809	29.0	68
$ 0\rangle \leftrightarrow 1-\rangle$	6.8566	25.5	52
$ 1-\rangle \leftrightarrow 2+\rangle$	6.8987	22.3	44
$ 1+\rangle \leftrightarrow 2-\rangle$	6.8402	18.9	48
$ 2-\rangle \leftrightarrow 3+\rangle$	6.9074	24.1	44
$ 2+\rangle \leftrightarrow 3-\rangle$	6.8315	19.4	32
$ 3-\rangle \leftrightarrow 4+\rangle$	6.9142	25.9	44
$ 3+\rangle \leftrightarrow 4-\rangle$	6.8246	22.0	24
$ 4-\rangle \leftrightarrow 5+\rangle$	6.9201	25.5	32
$ 5+\rangle \leftrightarrow 6-\rangle$	6.8143	22.7	—
$ 6-\rangle \leftrightarrow 7+\rangle$	6.9291	24.5	—

TABLE III. **Transition calibration parameters.** The table shows the frequency of each relevant transition and its respective maximum Rabi frequency Ω_s . Ω_s is defined as the coefficient of the $\frac{\Omega_s}{2}|(N+1)\mp\rangle\langle N\pm|$ matrix element when activated through the transmon drive with input signal voltage of 0.4 V. The parameter σ is the standard deviation of the Gaussian π pulse calibrated for each transition, with total duration of 4σ . The length of the $|5+\rangle \leftrightarrow |6-\rangle$ and $|6-\rangle \leftrightarrow |7+\rangle$ transitions were not optimized.

V. PREPARATION OF ARBITRARY BOSONIC STATES

We used the resonant control protocol to demonstrate the preparation of arbitrary states in the cavity with an analytical control sequence. The sequence consisted of activating the sidebands sequentially using variable-amplitude, Gaussian-shaped pulses with 4σ duration, where $\sigma \in [64, 96]$ ns. This method allows for straightforward preparation of any Fock state and their superpositions in the cavity, as shown in Fig. 11.

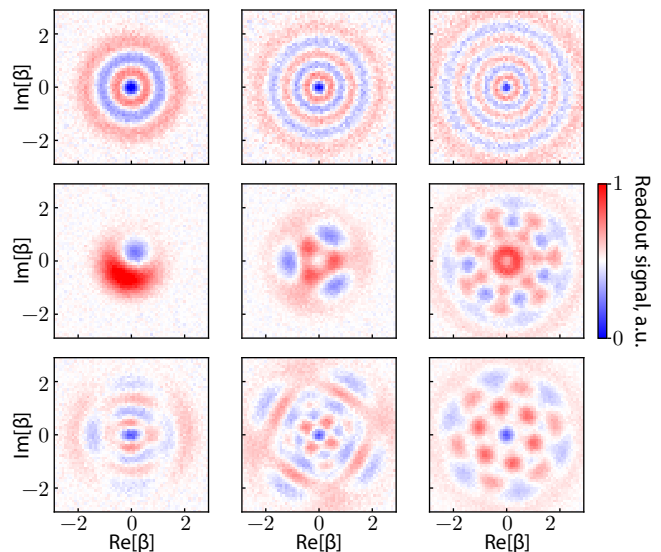


FIG. 11. **Qudit arbitrary state preparation.** Wigner plots showing diverse qudit states prepared by sequentially exciting sideband transitions in the Jaynes-Cummings ladder.

Due to a lack of appropriate quantum amplifier at the

specific moment of this experiment, we don't have single-shot readout of the transmon. Thus, the parity signal was calibrated by comparing it to a 1D Wigner measurement of cavity vacuum $|0\rangle$, which is independently measured beforehand. The Wigner plots closely resemble the target states in shape, though with a reduction in contrast. This indicates that the state preparation is mostly limited by the transmon decoherence.

VI. PARAMETRIC MODULATION

Although not required by the resonant control protocol, our device architecture is also capable of providing broadband parametric flux modulation of the SQUID.

We show this feature experimentally by using flux pumps to activate parametric resonances between the cavity and transmon with tunable strength. Sweeping the pump frequency ω_m around the transmon-cavity detuning of $\Delta/2\pi \approx 85$ MHz for a variable duration results in the continuous exchange of the transmon excitation with the cavity, as shown by the chevron pattern in Fig. 12(a). The resonant oscillations have a period of π/g_{eff} , where g_{eff} is the parametric coupling strength.

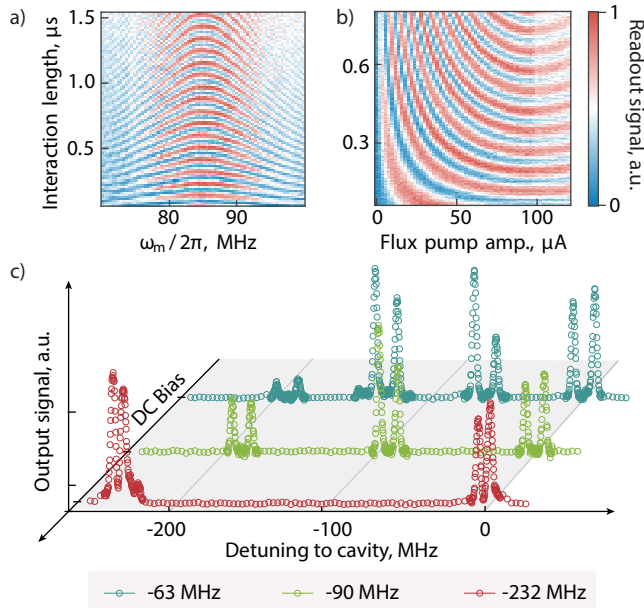


FIG. 12. **Protected flux-parametric modulation** (a) (b) (c) Qubit spectroscopy with the transmon parked at the cavity frequency with a flux pump $\Phi_e(t) = A \cos(\omega_m t)$ for variable A (converted to current) and $\omega_m/2\pi = 60$ MHz. The frequency split is compared to $g_{eff} = gJ_0 \left(\frac{2.4048}{90 \mu A} \times I \right)$, shown as a golden dashed line, where I is the current running through the coil.

The parametric coupling strength g_{eff} can be tuned on demand by changing the flux pump amplitude. Fig. 12(b) shows that the resonant oscillations become faster with larger flux pump amplitude (expressed in units of cur-

rent), corresponding to an increase in coupling strength. The pump amplitude I_p is estimated from the room-temperature input current after going through 26 dB attenuation and treating the flux line as a short. Fitting the oscillations to a cosine function for each pump amplitude indicates a variable $0 \leq g_{eff} \leq 6.6$ MHz. However, increasing the pump amplitude after the maximum coupling point leads to lower g_{eff} . This is consistent with the expected analytical trend $g_{eff} = g \times J_1(I_p/\nu)$, where g is the static coupling, J_1 is a Bessel function of the first kind and ν is proportionality factor [56].

The g_{eff} data extracted from Fig. 12(b) fits to the function $g_{eff}/2\pi = 11.3 \text{ MHz} \times J_1(I_p/53 \mu A)$, where I_p is in units of μA . The estimated coupling of $g = 11.3$ MHz is close to the value of 12.2 ± 0.1 MHz observed from the transmon-cavity avoided crossing. The factor ν can be calculated analytically using the formula

$$\nu = \left(\frac{2\pi}{\Phi_0} \frac{d\omega_T}{d\varphi_e} \frac{L}{\omega_m} \right)^{-1}, \quad (11)$$

where $\omega_T/2\pi = 6.783$ GHz is the transmon parking frequency and L is the effective mutual inductance with the SQUID. From the fitting value of $\nu = 53 \mu A$ we can calculate $L = 0.211 \Phi_0/\text{mA}$, which is considerably lower than the DC bias mutual inductance of $L_{DC} = 0.387 \Phi_0/\text{mA}$. This lower tunability can be partially attributed to the flux pump not fully driving the differential mode of the SQUID loop [57]. In further device iterations, the mismatch can be mitigated by incorporating a common-mode rejection filter on the flux line [34].

We test strong parametric resonances with flux pumps at higher modulation frequency. This is shown with transmon spectroscopy experiments at different parking detunings $\Delta = 63$ to 232 MHz under a continuous flux pump with frequency $\omega_m = \Delta$. The pump creates flux sidebands at frequencies $\bar{\omega}_T + N\omega_m$, where the average transmon frequency $\bar{\omega}_T$ approximately coincides with the parking frequency ω_T for low pump amplitudes. In all spectroscopy plots (Fig. 12(c)), the rightmost feature corresponds to the $N = 1$ sideband, which coincides with the cavity frequency and presents a frequency split corresponding to their avoided crossing. The next feature to the left corresponds to the transmon average frequency ($N = 0$), and the lower $N = -1$ and $N = -2$ sidebands can be seen within range of the spectroscopy for some DC biases. All features display the same frequency splitting indicating the strong coupling of the $N = 1$ sideband with the cavity for pump frequencies as high as 232 MHz.

VII. QUANTUM STATE RECONSTRUCTION

Here, we explain the procedure for reconstructing a quantum state, represented by its density matrix, with truncation dimension D , given the Wigner measurement data. An arbitrary D dimensional quantum state ρ is fully characterised by its $D^2 - 1$ independent real parameters, which we write in a vector form \vec{Y} . There are

many choices for the parametrisation of ρ . We take the first $D - 1$ diagonal elements of ρ as well as the $D^2 - D$ real and imaginary off-diagonal (upper triangular) elements. This way, the vector \vec{Y} consists of real elements, which fully characterise the density matrix ρ .

On the other hand, the Wigner measurement that we performed is expressed as $W(\alpha) = \text{tr}(\hat{P}\hat{D}(\alpha)\dagger\rho\hat{D}(\alpha))$ with $\hat{P} = e^{i\hat{a}\dagger\hat{a}\pi}$ being the parity operator and grid-based displacement points $\{\alpha\}$. Let us express all the Wigner data in a vector form \vec{X} . Consequently, the input state and Wigner data are related linearly, which can be written in a single matrix equation $\vec{X} = M\vec{Y} + \vec{V}$, where M and \vec{V} denote a mapping matrix and a constant vector, which can easily be computed given the choice of displacements $\{\alpha\}$.

The state reconstruction is carried out in a few steps. First, we performed linear inversion (LI) to get the estimated state parameters \vec{Y}_{est} , given the Wigner measurement data \vec{X} : $\vec{Y}_{\text{est}} = M^+(\vec{X} - \vec{V})$, where $M^+ = (M^\dagger M)^{-1}M^\dagger$ is the left Moore-Penrose pseudoinverse of the matrix M . Then, we construct the density matrix ρ_{LI} based on the estimated parameters. As errors are present in experiments, this density matrix might not be physical, i.e., it might contain negative eigenvalues. Finally, given ρ_{LI} , we employ Bayesian inference (explained in more detail below) to obtain a posterior probability distribution that accurately represent experimental data. From this distribution, we can sample density matrices and compute the mean fidelity and its standard deviation.

A. Bayesian inference

A popular technique to obtain a physical density matrix from experimental data in the presence of noise is maximum likelihood (ML), which gives us the closest physical density matrix ρ_{ML} from the obtained density matrix ρ_{LI} via linear inversion [58]. However, it is statistically less accurate. For example, it often leads to ρ_{ML} having zero eigenvalues [59, 60]. This is an issue as zero eigenvalues are interpreted as zero probabilities if we were to measure in the corresponding basis, which is not a valid conclusion as we perform finite measurement repetitions.

To address this issue, we use Bayesian inference, which is a statistically more accurate approach. Through Bayes' rule, it gives us a posterior distribution, explicitly showing uncertainty, given the measured experimental data (ρ_{LI}). The posterior distribution allows us to sample any functions of ρ (including itself). For exact implementation of Bayesian inference, we follow an efficient protocol proposed in Ref. [61]. When implementing the protocol, we use the following parameters: $\alpha = 1$, which establishes a uniform prior as we do not assume initial preference for the density matrix; the variance of the pseudo-likelihood $\sigma = 1/N$ with $N = \# \cdot (D^2 - 1)$

and $\#$ is the number of experimental repetition; we also generate 2^{10} Markov Chain Monte Carlo samples and apply a thinning parameter of 2^7 to mitigate correlations within the sample chain.

For example, we use the procedure to sample a large number of possible physical density matrices $\{\rho_{\text{BI},i}\}$ and compute their fidelities $F_i = (\text{tr}(\sqrt{\rho_{\text{BI},i}}\rho_{\text{tar}}\sqrt{\rho_{\text{BI},i}}))^2$ to a target state ρ_{tar} . The fidelity and its error presented in the main text are the average fidelity and its standard deviation.

VIII. PROTOCOL SIMULATION AND ERROR BUDGET

We estimate the effect of different error sources over the resonant control protocol by solving the master equation of the system.

First, we simulate the state preparation of states $|\psi_1\rangle = \frac{1}{\sqrt{2}}(|0\rangle + |3\rangle)$ and $|\psi_2\rangle = \frac{1}{2}|0\rangle + \frac{\sqrt{3}}{\sqrt{8}}(|2\rangle + |4\rangle)$ using sequential gaussian pulses to each transition. The system Hamiltonian was reconstructed using the experimentally calibrated transitions from Tab. III. The cavity lifetime $T_{1,\text{cav}}$, transmon lifetime T_1 and pure dephasing $T_\phi = \left(\frac{1}{T_2} - \frac{1}{2T_1}\right)^{-1}$ are implemented with the respective jump operators. The adiabatic decoupling is taken as ideal and implemented with a change of basis operation. The Wigner tomography executed in the dispersive regime is also reproduced in simulation with experimental parameters, namely a dispersive shift $\chi/2\pi = 1.62$ MHz, a parity-mapping time of 272 ns and gaussian $\pi/2$ pulses with $\sigma_{\pi/2}$ of 8 ns and total duration of 4σ . The simulated tomography is then rescaled following the amplitude of the Wigner function of vacuum obtained with consistent simulation parameters. The state fidelity is then estimated from density matrix reconstruction following the procedure described in Sect. VII.

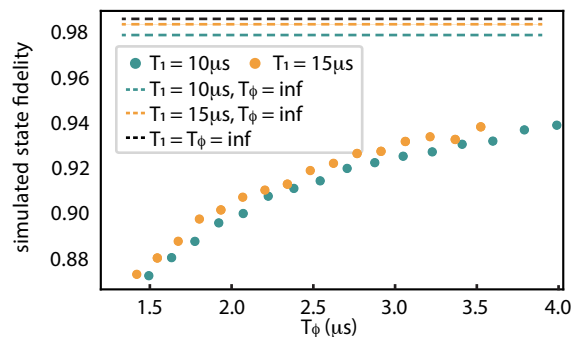


FIG. 13. **Simulated state preparation fidelities.** Simulated state fidelity of $|\psi_1\rangle = \frac{1}{\sqrt{3}}(|0\rangle + |3\rangle)$ as a function of transmon T_1 and T_ϕ .

The state preparation is simulated for transmon $T_1 = 10 \mu\text{s}$ and $15 \mu\text{s}$, and T_2 in the $[1.3, 2.8] \mu\text{s}$ range. The

cavity lifetime is fixed at $T_{1,\text{cav}} = 500 \mu\text{s}$. We first identify that the transmon is highly sensitive to changes in dephasing, as shown from the reconstructed fidelity as function of T_ϕ in Fig. 13: the fidelity of $|\psi_1\rangle$ varies in a large range [87.2%, 93.8%] ([87.3%, 93.8%]) for $T_1 = 10 \mu\text{s}$ ($15 \mu\text{s}$). These values also show the protocol is weakly sensitive to variations in transmon T_1 in this parameter range. Similar conclusions about T_1 and T_2 sensitivity can be drawn for state $|\psi_2\rangle$. Simulations with $T_2 = 2.7 \mu\text{s}$ and $T_1 = 15 \mu\text{s}$ ($T_\phi \approx 2.97 \mu\text{s}$) lead to 93.2% and 87.7% for states $|\psi_1\rangle$ and $|\psi_2\rangle$, respectively, which reproduce well the experimental fidelities of $93 \pm 3\%$ and $89 \pm 2\%$.

We calculate the fidelities of $|\psi_1\rangle$ and $|\psi_2\rangle$ while progressively including more sources of error in the simulation (Tab. IV). The results indicate that the dephasing T_ϕ has the largest impact in state preparation fidelity, followed by coherent errors due to finite pulse length, and transmon T_1 , in that order. From these simulations, we expect that the quality of state preparation can be significantly enhanced even with modest improvements in the transmon T_ϕ .

We simulate the Givens rotations between Fock states $|1\rangle$ and $|4\rangle$ using the same procedure, with the addition of the optimized $|1+\rangle \leftrightarrow |3-\rangle$ state transfer drive. The simulated cavity photon distributions are compared with the experimental reconstructed density matrix in Fig. 4c in the main text, showing a close match.

Simulations indicate that the experimental state fidelities after Givens rotations are significantly affected by coherent errors. When neglecting the transmon T_1 and T_2 , the state transfer $|1+\rangle \rightarrow |3-\rangle$ shows a fidelity of 95.0% when the system is initialized in $|1+\rangle$. For the same drive, the returning $|3-\rangle \rightarrow |1+\rangle$ path shows a fidelity of 85.8% when the system is initialized in $|3-\rangle$. We attribute these imperfections to the mismatch between the ideal Jaynes-Cummings model used in the drive optimization and the experimental Hamiltonian parameters, which leads to a difference on the order of ≈ 1 MHz in the frequencies of higher transitions. We expect that further improvements in our calibration and optimization methods will render significant improvement in the Givens rotations fidelities.

Included error sources	$ \psi_1\rangle$ fid. (%)	$ \psi_2\rangle$ fid. (%)
Finite pulse length	98.4	95.1
+ T_1	98.3	94.4
+ T_ϕ	93.2	87.7

TABLE IV. **Error budget for state preparation.** State fidelity for $|\psi_1\rangle = \frac{1}{\sqrt{2}}(|0\rangle + |3\rangle)$ and $|\psi_2\rangle = \frac{1}{2}|0\rangle + \frac{\sqrt{3}}{\sqrt{8}}(|2\rangle + |4\rangle)$ states with progressive addition of error sources.

-
- [1] P. W. Shor, Scheme for reducing decoherence in quantum computer memory, *Physical Review A* **52**, R2493–R2496 (1995).
- [2] S. Zhou, M. Zhang, J. Preskill, and L. Jiang, Achieving the heisenberg limit in quantum metrology using quantum error correction, *Nature Communications* **9**, 10.1038/s41467-017-02510-3 (2018).
- [3] H.-Y. Huang, Y. Tong, D. Fang, and Y. Su, Learning Many-Body Hamiltonians with Heisenberg-Limited Scaling, *Physical Review Letters* **130**, 200403 (2023).
- [4] E. Altman *et al.*, Quantum Simulators: Architectures and Opportunities, *PRX Quantum* **2**, 017003 (2021).
- [5] W. Hofstetter and T. Qin, Quantum simulation of strongly correlated condensed matter systems, *Journal of Physics B: Atomic, Molecular and Optical Physics* **51**, 082001 (2018).
- [6] D. A. Abanin *et al.*, Observation of constructive interference at the edge of quantum ergodicity, *Nature* **646**, 825–830 (2025).
- [7] B. P. Lanyon, M. Barbieri, M. P. Almeida, T. Jennewein, T. C. Ralph, K. J. Resch, G. J. Pryde, J. L. O’Brien, A. Gilchrist, and A. G. White, Simplifying quantum logic using higher-dimensional Hilbert spaces, *Nature Physics* **5**, 134–140 (2008).
- [8] Y. Wang, Z. Hu, B. C. Sanders, and S. Kais, Qudits and High-Dimensional Quantum Computing, *Frontiers in Physics* **8**:589504, 10.3389/fphy.2020.589504 (2020).
- [9] M. Rubin-Osanz, L. Bersani, S. Chicco, G. Allodi, R. De Renzi, A. Mavromagoulos, M. D. Roy, S. Piligkos, E. Garlatti, and S. Carretta, Implementation of the Quantum Fourier Transform on a molecular qudit with full refocusing and state tomography (2025), arXiv:2512.15611.
- [10] E. Moreno-Pineda, C. Godfrin, F. Balestro, W. Wernsdorfer, and M. Ruben, Molecular spin qudits for quantum algorithms, *Chemical Society Reviews* **47**, 501–513 (2018).
- [11] Y. Wang, S. Ru, F. Wang, P. Zhang, and F. Li, Experimental demonstration of efficient high-dimensional quantum gates with orbital angular momentum, *Quantum Science and Technology* **7**, 015016 (2021).
- [12] B. Kim, K.-M. Hu, M.-H. Sohn, Y. Kim, Y.-S. Kim, S.-W. Lee, and H.-T. Lim, Qudit-based variational quantum eigensolver using photonic orbital angular momentum states, *Science Advances* **10**, 10.1126/sciadv.ado3472 (2024).
- [13] P. J. Low, B. White, and C. Senko, Control and readout of a 13-level trapped ion qudit, *npj Quantum Information* **11**, 85 (2025).
- [14] X. Shi, J. Sinanan-Singh, T. J. Burke, J. Chiaverini, and I. L. Chuang, Efficient Implementation of a Quantum Algorithm with a Trapped Ion Qudit (2025), arXiv:2506.09371.
- [15] X. Yu, B. Wilhelm, D. Holmes, A. Vaartjes, D. Schwiendbacher, M. Nurizzo, A. Kringhøj, M. R. v. Blankenstein, A. M. Jakob, P. Gupta, F. E. Hudson, K. M. Itoh, R. J. Murray, R. Blume-Kohout, T. D. Ladd, N. Anand, A. S. Dzurak, B. C. Sanders, D. N. Jamieson, and A. Morello, Schrödinger cat states of a nuclear spin qudit in silicon, *Nature Physics* **21**, 362–367 (2025).

- [16] Z. Wang, R. W. Parker, E. Champion, and M. S. Blok, High- E_J/E_C transmon qudits with up to 12 levels, *Physical Review Applied* **23**, 034046 (2025).
- [17] P. Liu, R. Wang, J.-N. Zhang, Y. Zhang, X. Cai, H. Xu, Z. Li, J. Han, X. Li, G. Xue, W. Liu, L. You, Y. Jin, and H. Yu, Performing $SU(d)$ Operations and Rudimentary Algorithms in a Superconducting Transmon Qudit for $d = 3$ and $d = 4$, *Physical Review X* **13**, 021028 (2023).
- [18] E. Champion, Z. Wang, R. W. Parker, and M. S. Blok, Efficient Control of a Transmon Qudit Using Effective Spin-7/2 Rotations, *Physical Review X* **15**, 021096 (2025).
- [19] X. Deng, S. Li, Z.-J. Chen, Z. Ni, Y. Cai, J. Mai, L. Zhang, P. Zheng, H. Yu, C.-L. Zou, S. Liu, F. Yan, Y. Xu, and D. Yu, Quantum-enhanced metrology with large fock states, *Nature Physics* **20**, 1874–1880 (2024).
- [20] O. Milul, B. Guttel, U. Goldblatt, S. Hazanov, L. M. Joshi, D. Chausovsky, N. Kahn, E. undefinidyürek, F. Lafont, and S. Rosenblum, Superconducting Cavity Qubit with Tens of Milliseconds Single-Photon Coherence Time, *PRX Quantum* **4**, 030336 (2023).
- [21] A. Blais, A. L. Grimsmo, S. M. Girvin, and A. Wallraff, Circuit quantum electrodynamics, *Reviews of Modern Physics* **93**, 025005 (2021).
- [22] S. Krastanov, V. V. Albert, C. Shen, C.-L. Zou, R. W. Heeres, B. Vlastakis, R. J. Schoelkopf, and L. Jiang, Universal control of an oscillator with dispersive coupling to a qubit, *Physical Review A* **92**, 040303(R) (2015).
- [23] R. W. Heeres, B. Vlastakis, E. Holland, S. Krastanov, V. V. Albert, L. Frunzio, L. Jiang, and R. J. Schoelkopf, Cavity State Manipulation Using Photon-Number Selective Phase Gates, *Physical Review Letters* **115**, 137002 (2015).
- [24] R. W. Heeres, P. Reinhold, N. Ofek, L. Frunzio, L. Jiang, M. H. Devoret, and R. J. Schoelkopf, Implementing a universal gate set on a logical qubit encoded in an oscillator, *Nature Communications* **8**, 94 (2017).
- [25] J. Huang, T. J. DiNapoli, G. Rockwood, M. Yuan, P. Narasimhan, E. Gupta, M. Bal, F. Crisa, S. Garattoni, Y. Lu, L. Jiang, and S. Chakram, Fast Sideband Control of a Weakly Coupled Multimode Bosonic Memory (2025), arXiv:2503.10623.
- [26] T. Kim, T. Roy, X. You, A. C. Y. Li, H. Lamm, O. Pronitchev, M. Bal, S. Garattoni, F. Crisa, D. Bafia, D. Kurkuoglu, R. Pilipenko, P. Heidler, N. Bornman, D. van Zanten, S. Zorzetti, R. Harnik, A. Murthy, A. Lunin, S. Belomestnykh, S. Zhu, C. Wang, A. Vallières, Z. Huang, J. Koch, A. Grassellino, S. Chakram, A. Romanenko, and Y. Lu, Ultracoherent superconducting cavity-based multiqubit platform with error-resilient control (2025), arXiv:2506.03286.
- [27] L. Verney, R. Lescanne, M. H. Devoret, Z. Leghtas, and M. Mirrahimi, Structural instability of driven josephson circuits prevented by an inductive shunt, *Physical Review Applied* **11**, 024003 (2019).
- [28] Y. Lu, T. Zhao, A. Vallières, K. C. Smith, D. Weiss, X. You, Y. Zhang, S. Ganjam, A. Maiti, J. W. Garmon, *et al.*, Systematic construction of time-dependent hamiltonians for microwave-driven josephson circuits (2026), arXiv:2512.20743v3.
- [29] F. Valadares, N.-N. Huang, K. T. N. Chu, A. Dorogov, W. Chua, L. Kong, P. Song, and Y. Y. Gao, On-demand transposition across light-matter interaction regimes in bosonic cQED, *Nature Communications* **15**, 5816 (2024).
- [30] D. G. Atanasova, I. Yang, T. Hönlgl-Decrinis, D. Gusenkova, I. Pop, and G. Kirchmair, In situ tunable interaction with an invertible sign between a fluxonium and a post cavity, *PRX Quantum* **6**, 020318 (2025).
- [31] F. W. Strauch, All-Resonant Control of Superconducting Resonators, *Physical Review Letters* **109**, 210501 (2012).
- [32] D. I. Schuster, A. A. Houck, J. A. Schreier, A. Wallraff, J. M. Gambetta, A. Blais, L. Frunzio, J. Majer, B. Johnson, M. H. Devoret, S. M. Girvin, and R. J. Schoelkopf, Resolving photon number states in a superconducting circuit, *Nature* **445**, 515–518 (2007).
- [33] Supplementary materials.
- [34] Z. Li, E. Gupta, F. Zhao, R. Banerjee, Y. Lu, T. Roy, A. Oriani, A. Vrajitoarea, S. Chakram, and D. I. Schuster, A Cascaded Random Access Quantum Memory (2025), arXiv:2503.13953.
- [35] D. M. Pozar, *Microwave engineering: theory and techniques* (John Wiley & Sons, 2021).
- [36] T. Krisnanda, C. Y. Fontaine, A. Copetudo, P. Song, K. X. Lee, N.-N. Huang, F. Valadares, T. C. Liew, and Y. Y. Gao, Demonstrating efficient and robust bosonic state reconstruction via optimized excitation counting, *PRX Quantum* **6**, 010303 (2025).
- [37] T. Krisnanda, P. Song, A. Copetudo, C. Y. Fontaine, T. Paterek, T. C. Liew, and Y. Y. Gao, Experimental demonstration of enhanced quantum tomography via quantum reservoir processing, *Quantum Science and Technology* **10**, 035041 (2025).
- [38] G. K. Brennen, D. P. O’Leary, and S. S. Bullock, Criteria for exact qudit universality, *Physical Review A* **71**, 052318 (2005).
- [39] M. Hutchings, J. B. Hertzberg, Y. Liu, N. T. Bronn, G. A. Keefe, M. Brink, J. M. Chow, and B. Plourde, Tunable superconducting qubits with flux-independent coherence, *Physical Review Applied* **8**, 044003 (2017).
- [40] J. Braumüller, M. Sandberg, M. R. Vissers, A. Schneider, S. Schlör, L. Grünhaupt, H. Rotzinger, M. Marthaler, A. Lukashenko, A. Dieter, *et al.*, Concentric transmon qubit featuring fast tunability and an anisotropic magnetic dipole moment, *Applied Physics Letters* **108** (2016).
- [41] A. Eickbusch, V. Sivak, A. Z. Ding, S. S. Elder, S. R. Jha, J. Venkatraman, B. Royer, S. M. Girvin, R. J. Schoelkopf, and M. H. Devoret, Fast universal control of an oscillator with weak dispersive coupling to a qubit, *Nature Physics* **18**, 1464–1469 (2022).
- [42] S. Roy, A. Senanian, C. S. Wang, O. C. Wetherbee, L. Zhang, B. Cole, C. P. Larson, E. Yelton, K. Arora, P. L. McMahon, B. L. T. Plourde, B. Royer, and V. Fatemi, Synthetic High Angular Momentum Spin Dynamics in a Microwave Oscillator, *Physical Review X* **15**, 021009 (2025).
- [43] J. Koch, T. M. Yu, J. Gambetta, A. A. Houck, D. I. Schuster, J. Majer, A. Blais, M. H. Devoret, S. M. Girvin, and R. J. Schoelkopf, Charge-insensitive qubit design derived from the cooper pair box, *Physical Review A—Atomic, Molecular, and Optical Physics* **76**, 042319 (2007).
- [44] X. You, J. A. Sauls, and J. Koch, Circuit quantization in the presence of time-dependent external flux, *Physical Review B* **99**, 174512 (2019).
- [45] B. M. Terhal and D. Weigand, Encoding a qubit into a cavity mode in circuit qed using phase estimation, *Physical Review A* **93**, 012315 (2016).

- [46] C. Joshi, J. Larson, and T. P. Spiller, Quantum state engineering in hybrid open quantum systems, *Physical Review A* **93**, 043818 (2016).
- [47] G. Wang, R. Xiao, H. Shen, C. Sun, and K. Xue, Simulating anisotropic quantum rabi model via frequency modulation, *Scientific reports* **9**, 4569 (2019).
- [48] L. J. Henderson, R. Goel, and S. Shrapnel, Quantum kernel machine learning with continuous variables, *Quantum* **8**, 1570 (2024).
- [49] A. Yermeyev, A. Tolstobrov, G. Fedorov, S. Sanduleanu, P. Shlykov, S. Samarin, S. Kadyrmetov, A. Muraviev, A. Bolgar, D. Kalacheva, *et al.*, Variational preparation of entangled states in a system of transmon qubits, *Advanced Quantum Technologies*, e00316 (2025).
- [50] M. Reed, *Entanglement and quantum error correction with superconducting qubits* (Lulu. com, 2013).
- [51] O. Gargiulo, S. Oleschko, J. Prat-Camps, M. Zanner, and G. Kirchmair, Fast flux control of 3d transmon qubits using a magnetic hose, *Applied Physics Letters* **118** (2021).
- [52] F. Lecocq, C. Naud, I. M. Pop, Z.-H. Peng, I. Matei, T. Crozes, T. Fournier, W. Guichard, and O. Buisson, Novel e-beam lithography technique for in-situ junction fabrication: the controlled undercut, *arXiv preprint arXiv:1101.4576* (2011).
- [53] A. Copetudo, C. Y. Fontaine, F. Valadares, and Y. Y. Gao, Shaping photons: Quantum information processing with bosonic cqcd, *Applied Physics Letters* **124** (2024).
- [54] X. Pan, T. Krisnanda, A. Duina, K. Park, P. Song, C. Y. Fontaine, A. Copetudo, R. Filip, and Y. Y. Gao, Realization of versatile and effective quantum metrology using a single bosonic mode, *PRX Quantum* **6**, 010304 (2025).
- [55] L. V. Krayzman, *Thin-film 3D resonators for superconducting quantum circuits*, Ph.D. thesis, Yale University (2022).
- [56] N. Didier, E. A. Sete, M. P. da Silva, and C. Rigetti, Analytical modeling of parametrically modulated transmon qubits, *Physical Review A* **97**, 022330 (2018).
- [57] Y. Lu, A. Maiti, J. W. O. Garmon, S. Ganjam, Y. Zhang, J. Claes, L. Frunzio, S. M. Girvin, and R. J. Schoelkopf, High-fidelity parametric beamsplitting with a parity-protected converter, *Nature Communications* **14**, 5767 (2023).
- [58] J. A. Smolin, J. M. Gambetta, and G. Smith, Efficient method for computing the maximum-likelihood quantum state from measurements with additive gaussian noise, *Physical review letters* **108**, 070502 (2012).
- [59] R. Blume-Kohout, Optimal, reliable estimation of quantum states, *New Journal of Physics* **12**, 043034 (2010).
- [60] L. Knips, C. Schwemmer, N. Klein, J. Reuter, G. Tóth, and H. Weinfurter, How long does it take to obtain a physical density matrix?, *arXiv preprint arXiv:1512.06866* (2015).
- [61] J. M. Lukens, K. J. Law, A. Jasra, and P. Lougovski, A practical and efficient approach for bayesian quantum state estimation, *New Journal of Physics* **22**, 063038 (2020).